Characterization of the 14 June 2011 Norman, Oklahoma, Downburst through Dual-Polarization Radar Observations and Hydrometeor Classification

VIVEK N. MAHALE AND GUIFU ZHANG

School of Meteorology, and Advanced Radar Research Center, and Center for Analysis and Prediction of Storms, University of Oklahoma, Norman, Oklahoma

MING XUE

School of Meteorology, and Center for Analysis and Prediction of Storms, University of Oklahoma, Norman, Oklahoma

(Manuscript received 29 January 2016, in final form 2 September 2016)

ABSTRACT

On 14 June 2011, thunderstorms developed along a cold front in central Oklahoma in a thermodynamic environment that was conducive for downbursts. One of the thunderstorms produced a wet downburst in Norman, Oklahoma, that resulted in surface winds in excess of 35 m s^{-1} (>80 mi h^{-1}) and hailstones in excess of 4 cm in diameter. Unique 1-min observations of the downburst were recorded by an Oklahoma Mesonet station. These observations indicated a 6.6-hPa pressure rise that was coincident with a rain rate of 213 mm h^{-1} at the center of the downburst. In this event, both the research KOUN (Norman) and operational KTLX (Oklahoma City, Oklahoma) Weather Surveillance Radar-1988 Doppler (WSR-88D) instruments were scanning this downburst and its parent storm at close range (<30 km). KOUN provided polarimetric radar data (PRD) while both radars provided limited dual-Doppler coverage. The evolution of the downburst is analyzed mostly through the use of reconstructed range–height indicators of the PRD. A hydrometeor classification algorithm (HCA) is applied to the PRD to gain further understanding of the microphysical evolution of the downburst. Through the analyses, it is seen that graupel aloft made a transition to a nearly all rain and hail mixture above the 0°C level. This large area of mixed rain and hail eventually descended to the ground, causing the downburst. In this study, the HCA analyses are utilized to develop a conceptual model that characterizes the hydrometeor evolution of the parent downburst storm.

1. Introduction

Downbursts are areas of strong, damaging winds that are produced by intense convective downdrafts (Glickman 2000). Downbursts cause strong outflow winds at the surface (resulting in damage to structures on the ground) and are hazardous to aviation during the landing and takeoff stages of aircraft flight (Fujita and Caracena 1977; National Transportation Safety Board 1983; Fujita 1985, 1986). Downbursts have been classified by diameter and precipitation amount (e.g., Wakimoto 2001). Microbursts are ≤4 km in diameter and usually have winds that last 2–5 min. Macrobursts are >4 km in diameter, and have winds that last 5–20 min. Typically, dry–low-reflectivity downbursts have <0.25-mm rainfall at the surface or a radar echo <35 dBZ in intensity, and wet downbursts have >0.25-mm rainfall at the surface or a radar echo >35-dBZ intensity; wet downbursts may also have hail in addition to rain. The ambient environments and microphysical processes for dry and wet downbursts have been found to be different (e.g., Wakimoto 2001); however, there can be some overlap between the dry and wet downburst ambient environments and microphysics. Downbursts that occur with overlapping characteristics sometimes are known as hybrid downbursts (Warning Decision Training Division 2016).

Much of the current understanding on downbursts was obtained from observation-based studies (e.g., Wakimoto and Bringi 1988; Wakimoto et al. 1994; Atlas et al. 2004) and from idealized numerical simulations (e.g., Srivastava 1985, 1987; Proctor 1988, 1989). Wakimoto (2001) and Wilson and Wakimoto (2001) summarized the related

---

Corresponding author e-mail: Vivek N. Mahale, vmahale@ou.edu

DOI: 10.1175/JAMC-D-16-0062.1

findings. From these studies, it is understood that precipitation microphysical processes in a suitable ambient thermodynamic environment are important in producing downbursts. For dry downbursts, the sublimation of snowflake particles through a deep, dry adiabatic layer has shown to be effective in producing downbursts (Proctor 1989; Wakimoto et al. 1994). For wet downbursts, the ambient thermodynamic environment is more humid and stable. In these situations, precipitation loading becomes more important for driving the initial downdraft at midlevels. As the environmental lapse rate decreases (increases), higher (lower) water content is needed for a downburst (Srivastava 1985). Observations and simulations also suggest that melting hailstones are important for wet downbursts (e.g., Srivastava 1987; Wakimoto and Bringi 1988; Proctor 1989; Atlas et al. 2004; Fu and Guo 2007). Fu and Guo (2007) simulated a downburst using a three-dimensional cloud model that included hail-bin microphysics. They found that the downburst primarily was produced by hail loading and was enhanced by cooling processes that were due to melting hailstones and the evaporation of raindrops. Dry downbursts tend to have a small negative temperature perturbation (i.e., cooling) over a deep column. In contrast, wet downbursts tend to have a relatively larger negative temperature perturbation over a shallower column near the surface (Proctor 1989). Proctor (1989) found warming aloft with wet downbursts, indicating that precipitation loading is necessary to overcome positive temperature buoyancy. The large cold pool near the surface may also enhance outflow winds in wet downbursts because of horizontal pressure gradient forces by the presence of a mesohigh underneath the cold pool (Wilson and Wakimoto 2001). The cold pool would spread in the form of a strong density current.

Downbursts were heavily studied in the 1970s and 1980s because of significant impacts on aviation (e.g., Fujita and Caracena 1977; National Transportation Safety Board 1983; Fujita 1985, 1986). In 1985, the crash of Delta flight 191 at the Dallas–Fort Worth (Texas) airport led the Federal Aviation Administration (FAA) to conduct a study on how dangerous, low-level wind shear could be detected (Whiton et al. 1998). The result was funding by Congress for the C-band Terminal Doppler Weather Radar (TDWR) program. The TWDR program is separate from the program that developed the national Weather Surveillance Radar-1988 Doppler (WSR-88D) S-band radar network, also known as the Next Generation Radar (NEXRAD). The FAA provided funding for research scientists to advance automated algorithms for microburst and/or wind shear detection using TDWR (e.g., Evans and Turnbull 1989; Merritt et al. 1989).

The WSR-88D network has recently been upgraded to have dual-polarization (dual-pol) capabilities, and the polarimetric radar data (PRD) provide an opportunity to study downburst microphysics and dynamics. In addition to the reflectivity at horizontal polarization Z_H (hereinafter reflectivity), the polarimetric WSR-88D estimates differential reflectivity Z_{DR}, differential phase Φ_{DP}, and copolar correlation coefficient ρ_{hv}.

By using the PRD, a better understanding of the microphysical evolution of precipitation is possible. For downbursts, a limited number of studies have utilized dual-pol radar observations (e.g., Wakimoto and Bringi 1988; Scharfenberg 2003; Atlas et al. 2004; Suzuki et al. 2010; Richter et al. 2014; Kuster et al. 2016). Wakimoto and Bringi (1988) conducted a study from data collected during the Microburst and Severe Thunderstorm (MIST) project. In their study, they found near-zero Z_{DR} surrounded by positive Z_{DR} in the main precipitation core within a microburst-producing downdraft; they determined that this "Z_{DR} hole" is associated with a strong downdraft composed of melting hail. Wakimoto and Bringi (1988) did not utilize ρ_{hv} or any aggregated quantities in their study. Atlas et al. (2004) also utilized Z_{DR} to track hail for a wet microburst event. Scharfenberg (2003) and Suzuki et al. (2010) both noted a decrease of ρ_{hv} in a downburst storm. The decrease of ρ_{hv} was attributed to mixed-phase hydrometeors, that is, mixture of rain and hail, in the downburst.

Hydrometeor classification algorithms (HCAs) have used PRD to classify radar echoes for different hydrometeors and nonmeteorological scatterers (e.g., Straka and Zrnić 1993). HCAs are usually based upon fuzzy logic, and the classification techniques have become more sophisticated in recent years (e.g., Zrnić and Ryzhkov 1999; Vivekanandan et al. 1999; Liu and Chandrasekar 2000; Straka et al. 2000; Zrnić et al. 2001; Lim et al. 2005; Park et al. 2009). HCAs aggregate different radar variables to determine the different hydrometeor classes, which can reveal the evolution of storm microphysics.

In this study, the microphysical evolution of a downburst is analyzed primarily through the use of the dual-pol WSR-88D (KOUN) instrument located in Norman, Oklahoma. The downburst affected Norman in the early evening between 1929 and 1950 central daylight time (CDT) 14 June 2011 (0029–0050 UTC 15 June 2011). This study builds upon previous work from Mahale et al. (2013) and complements an analysis of this storm by Kuster et al. (2016) that utilized 1-min phased-array radar (PAR) and KOUN radar data. In Mahale et al. (2013), a simplified HCA was used to provide a brief analysis of the 14 June downburst. In this paper, a more advanced HCA is utilized to develop a conceptual model that characterizes the hydrometeor evolution of the parent downburst storm.

This study is unique for being the first to analyze the evolution of a downburst through the use of an HCA.

The data and tools for this study are described in section 2. This is followed by an overview of the downburst event in section 3. Next, reconstructed range–height indicator (RHI) analyses of polarimetric radar observations and HCA in the beginning through latter stages of the thunderstorm along with dual-Doppler analyses are given in section 4. Discussion and conclusions for the study are provided in the last section. A comparison with Kuster et al. (2016) also is provided in the conclusion section.

2. Data and tools

a. Data sources

The KOUN S-band (~11.09 cm) WSR-88D collected polarimetric radar observations of the downburst and its parent thunderstorm. The National Weather Service (NWS) installed on the KOUN radar (of the National Severe Storms Laboratory) the prototype dual-polarization upgrade for the WSR-88D (Saxion and Ice 2012). The radar has a beamwidth of 0.925° and a range resolution of 230 m. Moment data are estimated at the range spacing of 250 m, and the azimuth increment is 0.5° for the lowest two elevation scans (0.5° and 1.5°). The two lowest elevation angles are split cut elevations, where there is a low PRF contiguous surveillance (CS) and high PRF contiguous Doppler (CD) scan. Reflectivity and PRD are processed from the CS scan. At higher elevations, the azimuth increment is 1.0°. KOUN was scanning with volume coverage pattern (VCP) 11, which was a VCP frequently used for severe thunderstorms in the past (Office of the Federal Coordinator for Meteorological Services and Supporting Research 2011). In this scanning strategy, each volume scan takes approximately 5 min and includes 360° plan position indicator (PPI) scans (i.e., conical scans) collected at 14 different elevations. The PPI scans are taken at approximately 0.5°, 1.5°, 2.4°, 3.4°, 4.3°, 5.3°, 6.2°, 7.5°, 8.7°, 10.0°, 12.0°, 14.0°, 16.7°, and 19.5° elevation angles. The KOUN radar was within 5 km of the downburst, providing excellent resolution and low-level coverage for this event. However, because the highest elevation PPI was at 19.5°, a limitation is the storm top was not sampled because of the radar cone of silence. As the storm approached the radar, less of the storm was sampled aloft. WSR-88D data were obtained from the National Climatic Data Center (NOAA/NCDC 2011a).

Surface observations were provided by the Oklahoma Mesonet, which is maintained by the Oklahoma Climatological Survey (2011). The Oklahoma Mesonet (Brock et al. 1995; McPherson et al. 2007) is a network of over 100 automated weather stations covering Oklahoma. There is a mesonet station in Norman that is nearly collocated with the KOUN radar. The mesonet station recorded 1-min data from the downburst. The data collected include temperature and relative humidity at 2 m, wind speed and direction at 10 m, station atmospheric pressure, and tipping-bucket precipitation. One tip is equivalent to 0.254 mm of rainfall. The 10-m maximum wind speed (i.e., wind gust) is the highest 3-s sample within the 1-min interval. The unique 1-min temporal resolution provides highly detailed information about the surface conditions beneath the downburst.

b. Modified HCA

The basis of the HCA used in S-band WSR-88D systems was developed by Park et al. (2009, hereinafter P09) and is based upon the fuzzy-logic method. The P09 HCA distinguishes among 10 classes of radar echoes: 1) ground clutter and anomalous propagation (GC/AP); 2) biological scatterers (BS); 3) dry aggregated snow (DS); 4) wet snow (WS); 5) crystals (CR); 6) graupel (GR); 7) big drops (BD); 8) light and moderate rain (RA); 9) heavy rain (HR); 10) a mixture of rain and hail (RH).

In this study, a modified version of the P09 HCA as described in Mahale et al. (2014) is used for analysis of the microphysical evolution. The methods and products of the HCA in Mahale et al. (2014) are described in the following paragraphs with modifications. This HCA was chosen because a version of it is implemented on the WSR-88D network. Mahale et al. (2014) made simplifications to the original algorithm that include 1) no use of K_{DP}, 2) no attenuation correction for Z_H or Z_{DR}, and 3) no confidence vectors. These simplifications are made because of varied methods and uncertainty in K_{DP} calculations and attenuation correction, and the need to determine confidence vectors. Mahale et al. (2014) found the results from these simplifications are fairly "similar to those of the operational algorithm used to produce the HCA categories in the level-3 WSR-88D data" (Mahale et al. 2014, p. 2019). Therefore, the five variables used for the discrimination of hydrometeors and nonmeteorological scatterers are 1) Z_H, 2) Z_{DR}, 3) ρ_{hv}, 4) a texture parameter SD(Z_H), and 5) another texture parameter SD(Φ_{DP}).

The classification of the radar echo is determined by which class has the largest aggregation value, which is dependent on what hydrometeors provide the dominant signal within a radar resolution volume (i.e., radar gate). Therefore, it is reasonable to assume there possibly could be a mix of hydrometeors in a radar resolution volume even outside the mixture of rain and hail

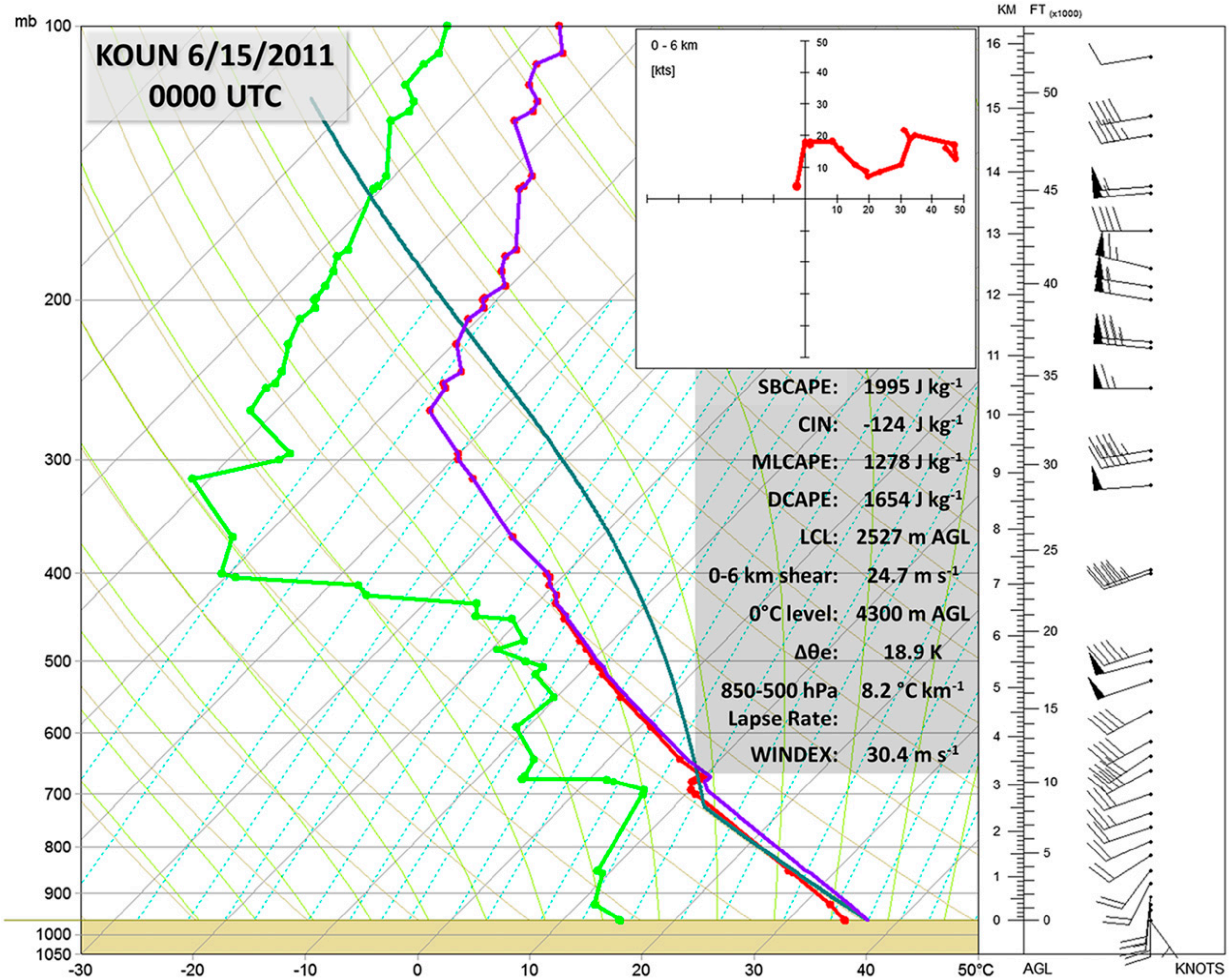

FIG. 1. Upper-air sounding and hodograph from Norman (KOUN) at 0000 UTC 15 Jun 2011. Temperature is denoted by the red line, and dewpoint is shown by the green line. The purple line is the virtual temperature correction, and the turquoise line represents the parcel path for surface-based parcel. Data were plotted using the Universal Rawinsonde Observation (raob) program.

classification. One hydrometeor may serve as an embryo for a different hydrometeor. For example, Harimaya (1976) found both snow crystals and frozen drops as center particles for graupel particles. It is understood that graupel develops as supercooled water droplets freeze on contact with snow crystals (i.e., riming; Lamb and Verlinde 2011). Thus, in regions of graupel formation, supercooled droplets and snow crystals would be expected to be present as well. This is an example where the HCA could give insight into the ongoing microphysical processes within the storm.

As described in Mahale et al. (2014), the depth of the melting layer can be estimated using the height of reduced ρ_{hv} rings in higher elevation PPI scans. Automated melting-layer detection algorithms (e.g., Brandes and Ikeda 2004; Giangrande et al. 2008) utilize reduced ρ_{hv} to help determine the melting layer. For example, Giangrande et al. (2008) used ρ_{hv} values between 0.90 and 0.97 as a starting point in their algorithm. Therefore, using reduced ρ_{hv} rings should provide similar results to automated algorithms. The top of the melting layer (i.e., the estimated 0°C level) is the height associated with the farthest distance of the ρ_{hv} ring, which was close to the height of the 0°C level on the observed sounding (Fig. 1) in this study (~4.3 km above ground level). The bottom of the melting layer is the height associated with the closest distance of the ρ_{hv} ring. Therefore, the radial extent of the ρ_{hv} ring is proportional to the depth of the melting layer. The following restrictions are placed on classes based upon the melting layer: 1) above the 0°C level, the only classes allowed are DS, CR, GR, and RH; 2) within the melting layer, the only class not allowed is BS; and 3) below the melting layer, the only classes allowed are GC/AP, BS, BD, RA, HR, and RH.

Otherwise, as noted in Mahale et al. (2014), the membership functions, weights, and hard thresholds are the same as implemented in P09. For PPIs, a 9-point median filter of the raw classifications is done to account for errors in the HCA output and noise in the level 2 radar data. For reconstructed RHIs, a 3-point median filter of the raw classifications is done radially.

In addition, quality control was done on the reconstructed RHI radar data for this event. The default signal-to-noise (SNR) reflectivity threshold for WSR-88D data is 2 dB (Melinikov and Zrnić 2007). In other words, reflectivity is only calculated where SNR is estimated to be larger than 2 dB. Using this threshold, the range-dependent minimum detectable reflectivity was estimated by calculating the azimuthal median reflectivity on the extreme peripheral of some precipitation. The median reflectivity was assumed to be representative of the minimum detectable reflectivity at that range. The reflectivity estimate was then extrapolated for the entire range of the radar observations. This allowed for the estimation of the SNR for the entire radar domain, which is not provided in the level 2 radar data. Melinikov and Zrnić (2007) found that Z_{DR} and ρ_{hv} are susceptible to bias for SNR interval of 2–15 dB. Data where SNR were less than 17 dB (i.e., radar data that were 15 dB greater than the minimum detectable reflectivity) were removed to reduce the influence of noise. The additional 2 dB adds a margin for error without sacrificing data in the downburst region of the thunderstorm.

3. Event overview

a. Mesoscale environment and evolution

The thermodynamics of the atmosphere were highly conducive for storms to produce severe downbursts in central Oklahoma on 14 June. The Norman (KOUN) sounding at 0000 UTC 15 June 2011 was the closest spatiotemporal sounding to the downburst (Fig. 1). The downburst affected Norman just after 0020 UTC; therefore, the sounding should be a reasonable representation of the prestorm environment.

As shown by the calculated parameters, the atmosphere was favorable for organized severe thunderstorms with both moderate instability and vertical wind shear. A nearly dry adiabatic (well mixed) layer existed below the cloud layer, which is favorable for downbursts (Srivastava 1987) and results in large downdraft convective available potential energy (DCAPE). DCAPE is defined as the maximum increase in kinetic energy (per unit mass) that could result from evaporative cooling from some height to the surface (Emanuel 1994). Note that this sounding is not a classic wet downburst sounding (i.e., Atkins and Wakimoto 1991) because of the relatively dry boundary layer.

Two parameters that specifically have been computed to assess downburst potential are the $\Delta\theta_{\mathrm{e}}$ between the near-ground maximum and the midlevel minimum (Atkins and Wakimoto 1991) and the wind index (WINDEX; McCann 1994). The $\Delta\theta_e$ of 18.4 K is lower than the 20-K threshold for wet downbursts found in Atkins and Wakimoto (1991); however, this could be attributed to not being a classic wet downburst sounding. Finally, the WINDEX was calculated to be 30.4 m s^{-1} (59 kt), which underestimated the >35 m s^{-1} surface winds measured.

On the mesoscale, a cold front was located across central Oklahoma (Fig. 2). The temperature change across the cold front was weak [~(3°–4°C)]. The wind shift along the cold front was nearly 180°; thus, surface convergence was present along the boundary. The convergence along the cold front was also detected by the KTLX (Oklahoma City, Oklahoma) WSR-88D; a weak line of reflectivity indicated a buildup of particulates and insects along the convergence line. The thunderstorm that would produce the downburst initiated just ahead of a cold front, near the Minco mesonet site due west of the Norman site, around 2315 UTC 14 June 2011 (Figs. 2a,b).

Initially, the storm motion was northeastward, parallel to the cold front. The thunderstorm rapidly intensified between 2315 and 2345 UTC (Figs. 2a,b). By 2345 UTC, the thunderstorm began to split into two cells. The Minco mesonet station experienced an 8°C decrease in temperature and a 5°C increase in dewpoint as the storm passed by between 2335 and 2355 UTC (not shown). The left split had a storm motion that was predominantly northward; the right split had an east-southeastward storm motion. The right split was the thunderstorm that would produce a downburst in Norman (cf., Fig. 2c).

b. Surface observations of the downburst

Figure 3 shows the 1-min Norman mesonet data plots from 2330 to 0130 UTC. Initially, the station pressure was steady at ~963.5 hPa from 2330 to 2350 UTC. After 2350 UTC, there was a steady decrease of pressure until 0013 UTC. The gust front passed by the mesonet station at 0025 UTC, when the wind speed at the station increased from below 10 to over 30 m s^{-1} in about 5 min. The gust front represents the leading edge of the outflow from the ambient air. It is speculated that the pressure decrease ahead of the gust front was dynamically induced by converging and rising air along the leading edge of the gust front. With the gust-frontal passage, the

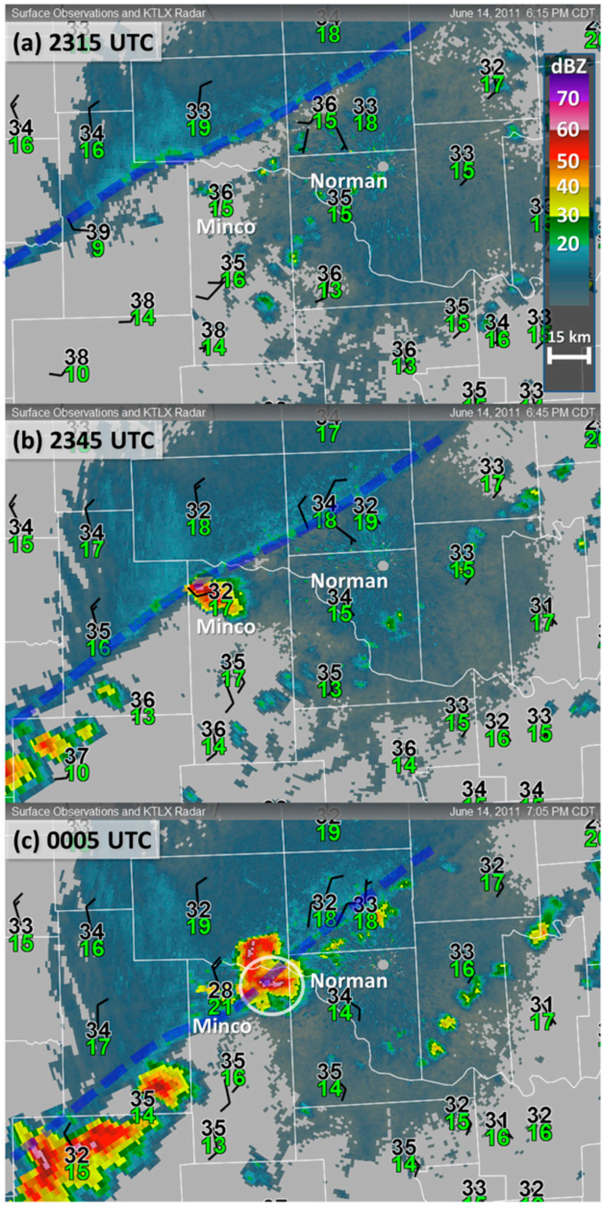

FIG. 2. KTLX radar reflectivity (dBZ) and Oklahoma Mesonet surface observations valid at (a) 2315, (b) 2345, and (c) 0005 UTC. Surface temperature (°C; black), dewpoint (°C; green), and wind (full barb ≡ 5 m s^{-1}; half barb ≡ 2.5 m s^{-1}) are plotted. The white circle in (c) highlights the storm that would produce the downburst. The dashed blue line is the approximate location of the cold front. The location of the Norman and Minco mesonet stations are indicated. Data were plotted using WeatherScope.

temperature decreased from 34°C at 0025 UTC to 22°C at 0033 UTC, which was accompanied by a relative humidity increase from 34% to 94%. Thereafter, the temperature and relative humidity remained nearly steady state with only slight fluctuations. The decrease in temperature and increase in relative humidity behind the gust front were due to melting hailstones and evaporating raindrops, which remove latent heat from the atmosphere (i.e., diabatic cooling). The maximum wind gust was 31.5 m s^{-1} from the northwest (322°) at 0029 UTC. A severe thunderstorm has wind gusts greater than or equal to 25.7 m s^{-1} (NWS 2014). Therefore, the wind speed and the accompanying features qualify the event as a severe downburst.

Rain began to fall at the station between 0029 and 0030 UTC. Another wind gust of 31.3 m s^{-1} occurred at 0033 UTC. The rain rate rapidly increased to 168 mm h^{-1} between 0032 and 0033 UTC. The atmospheric pressure increased to 966.6 hPa at 0034 UTC; however, the pressure decreased thereafter until 0036 UTC. The rain rate peaked at 213 mm h^{-1} (~8.4 in h^{-1}) between 0037 and 0038 UTC. The peak rain rate was coincident with an atmospheric pressure of 967.9 hPa at 0038 UTC, which was the maximum atmospheric pressure during the event. Note that this maximum is the 1-min average atmospheric pressure using a sampling period of 12 s. The maximum 12-s sample of atmospheric pressure within that minute was 968.7 hPa (not shown). The minimum (1-min average) atmospheric pressure was 961.3 hPa at 0013 UTC. The minimum 12-s atmospheric pressure within that minute was 961.2 hPa (not shown). Therefore, there was a 6.6-hPa increase in (1-min average) pressure in 15 min.

Typically, a downburst is defined by strong outflow winds at the surface; however, the center of the mesohigh associated with the cold pool is a better representation of the downdraft location. For example, Proctor (1989) found a pressure dome beneath the downdraft in his numerical simulation of a microburst. Therefore, the maximum atmospheric pressure (i.e., the center of the downburst) being coincident with the peak rain rate indicates precipitation loading was a cause of this wet downburst. Several additional wind gusts of ≥20 m s^{-1} occurred until 0050 UTC. The final downburst-related wind gust was 25 m s^{-1} from the east-southeast (108°) at 0050 UTC. Note that the wind direction switched ~150° from beginning to end, indicating the station experienced outflow from opposite sides of the downburst. This is reasonable because the pressure maximum and large rain rate suggest the center of the downburst passed over or close to the Norman mesonet station. The presence of several wind gust surges and a secondary pressure maximum suggest the downburst event was the aggregation of several downdraft surges or pulses within the storm. Downdraft surges previously were documented in 1-min Oklahoma Mesonet data during the 17 August 1994 Lahoma, Oklahoma, windstorm (Morris and Shafer 1996) and have been well documented in rear-flank downdrafts associated with supercell thunderstorms

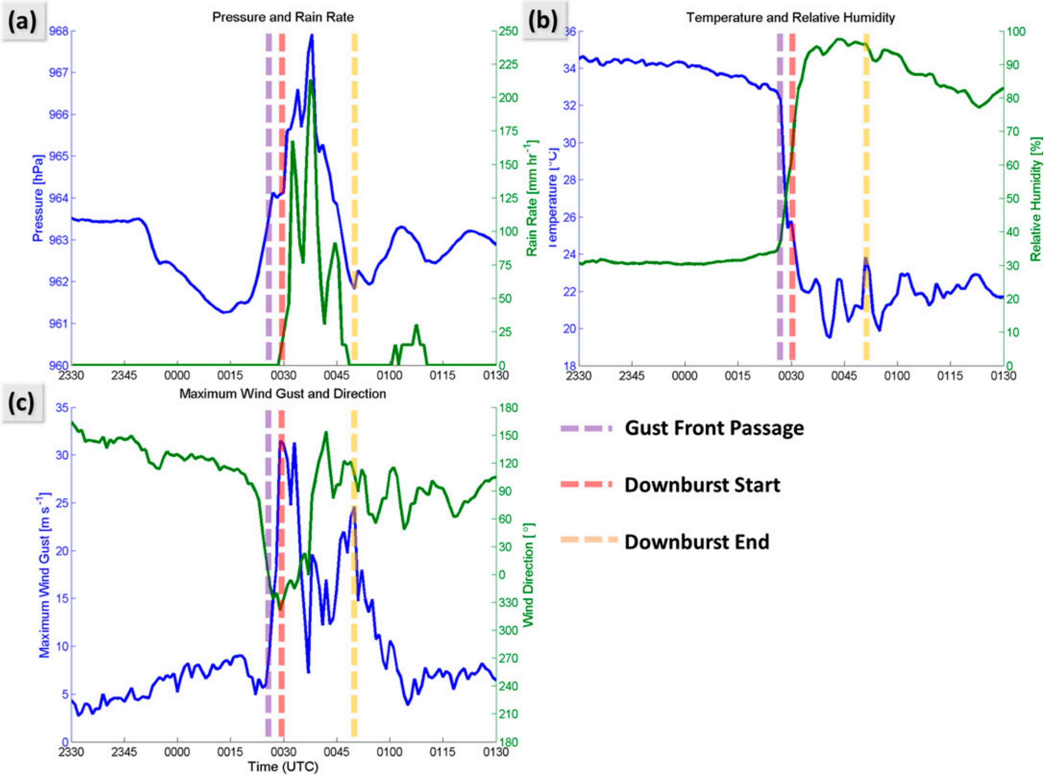

FIG. 3. The 1-min Oklahoma Mesonet data at Norman of (a) surface pressure (hPa) and rain rate (mm h^{-1}), (b) 2-m temperature (°C) and 2-m relative humidity (%), and (c) 10-m maximum wind gust (m s^{-1}) and wind direction (°) valid from 2330 to 0130 UTC. The times of the gust-frontal passage, downburst start, and downburst end are noted by the vertical dashed lines.

(e.g., Marquis et al. 2008; Wurman et al. 2010; Skinner et al. 2011; Kosiba et al. 2013).

Figure 4 summarizes the observations of the downburst at the Oklahoma Mesonet station. The start and end times of the downburst event at the Oklahoma Mesonet are defined by the first and last wind gust ≥ 20 m s^{-1}. Therefore, the start time is 0029 UTC and the end time is 0050 UTC.

c. Damage reports from the downburst

Surface winds in excess of 35 m s^{-1} (>80 mi h^{-1}) and hailstones in excess of 4 cm in diameter were reported from the storm in Norman (NOAA/NCDC 2011b). The maximum wind gust measured was 36.7 m s^{-1} in southeast Norman, and the largest hailstone reported was 4.4 cm. The maximum wind gust may have been underestimated because the anemometer recorded the 36.7 m s^{-1} before malfunctioning because of windblown hail. As a result of the downburst, widespread wind damage occurred across Norman (Fig. 5a), including at Max Westheimer Airport (Figs. 5b,c). Numerous power lines were snapped and over 33 000 residents of Norman lost power; some residents lost power for over 24 h. Nearly horizontal, windblown hailstones damaged automobiles, house siding, and store signs. The area of damage from the downburst was over 4 km in length; therefore, the downburst can be classified a macroburst by size.

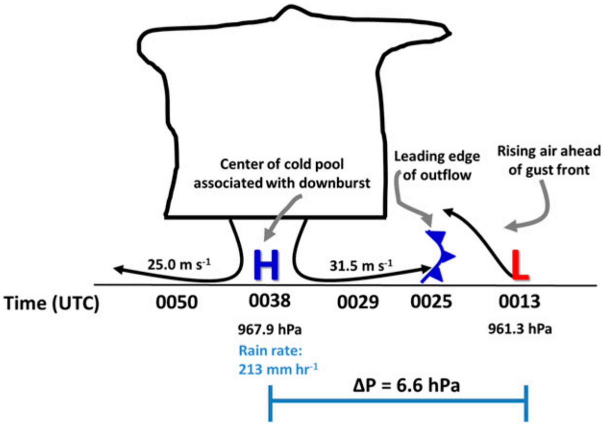

FIG. 4. Time evolution of surface observations as the downburst passed over the Oklahoma Mesonet station at Norman. Time-relative maximum and minimum surface pressure are noted by H and L respectively. The gust-frontal passage is noted by the cold-front symbol. The schematic is based upon 1-min data from Fig. 3.

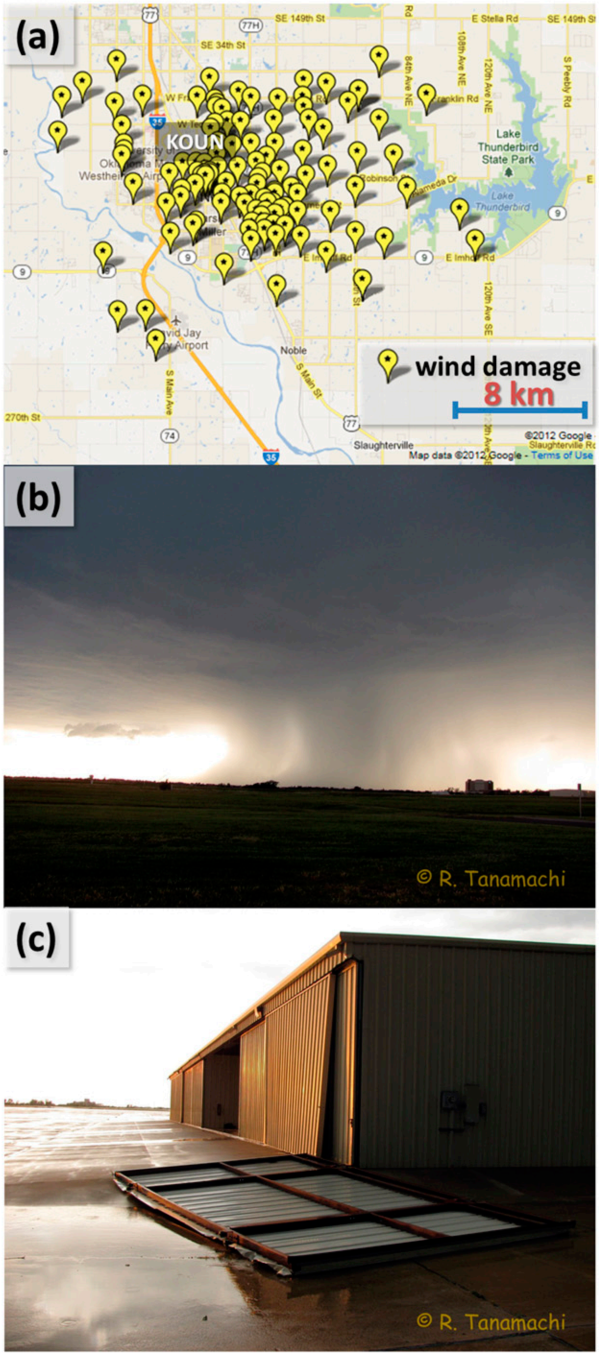

FIG. 5. (a) Map of wind-damage reports (provided through the courtesy of the NWS Norman), (b) a photograph of the downburst taken from north Norman, and (c) a photograph of damage at Max Westheimer Airport. The photographs are provided through the courtesy of Robin Tanamachi.

4. Polarimetric radar observations

One way to gain understanding on the storm microphysics associated with the downburst is to study the spatiotemporal changes in both the dual-pol variables and the output of the HCA in the parent thunderstorm. The azimuths for these reconstructed RHIs were subjectively selected through the most intense part of the thunderstorm for each volume scan.

In the developing stage of the storm, there was a Z_{DR} column that existed above the melting layer of ~4.3 km (Fig. 6a). The Z_{DR} columns indicate the presence of liquid or mixed-phase oblate hydrometeors being lofted above the 0°C level by the storm updraft (e.g., Hall et al. 1984; Kumjian and Ryzhkov 2008; Kumjian et al. 2012). Therefore, the Z_{DR} column can be considered a proxy for the updraft location within the storm; however, the Z_{DR} column could be slightly offset from the most intense portion of the updraft (e.g., Loney et al. 2002). The Z_{DR} columns that penetrate above the 0°C level indicate the presence of a very strong updraft (Kumjian et al. 2012). In the 2333–2337 UTC volume scan (Fig. 6a), the Z_{DR} column extended to at least 6.5 km above radar level (ARL), or ~2.2 km above the 0°C level, with a Z_{DR} estimate of 2.6 dB at the top of the column. The deep Z_{DR} column indicates that the storm had a relatively intense updraft. There was also a low ρ_{hv} column collocated with the Z_{DR} column, suggesting mixed hydrometeors were present within the updraft column. The HCA output (Fig. 7a) indicates primarily graupel with some rain and hail mixture within and above the Z_{DR} column. Although the HCA may only list graupel for its output, other hydrometers, such as supercooled droplets and snow crystals, probably are present in regions denoted as graupel because they are necessary for the formation of graupel (e.g., Pruppacher and Klett 1997). There was also a column of decreased inbound radial velocities collocated within the Z_{DR} column, which is further confirmation that the flow was more vertical rather than horizontal within this portion of the storm.

In the 2338–2342 volume scan (Fig. 6b), the Z_{DR} column maintained itself to at least 6.0 km ARL, or 1.7 km above the 0°C level. The HCA output (Fig. 7b) indicates that the area of graupel had transitioned to primarily rain and hail mixture within and above the Z_{DR} column. An overall increase of radar reflectivity ≥ 50 dBZ within and above the Z_{DR} column is the primary reason why the HCA output indicates the presence of more rain and hail mixture than in the previous volume scan. Hailstones have two different precursors (i.e., hail embryos) for development, which are frozen-drop embryos or graupel embryos (Knight 1981). The embryo type depends on the depth of the layer in which the warm-cloud process of collision–coalescence may occur (i.e., the depth of the >0°C region within the storm); the shallower the warm-cloud region, the more likely that hailstones will develop from graupel embryos. In this

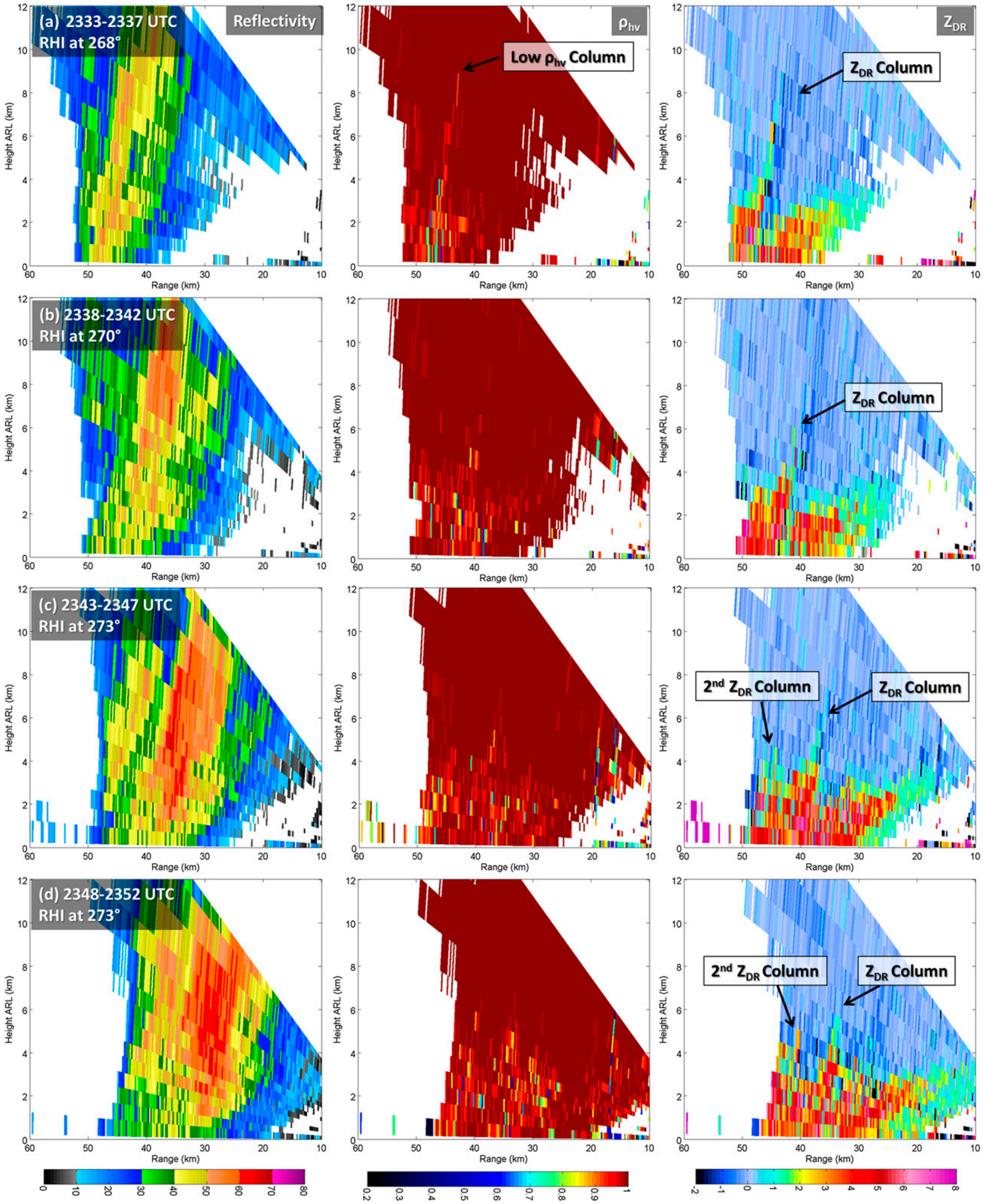

FIG. 6. Reconstructed RHI analyses from KOUN. Horizontal radar reflectivity factor Z_H, copolar correlation coefficient ρ_{hv}, and differential reflectivity Z_{DR} are shown at (a) 2333–2337, (b) 2338–2342, (c) 2243–2347, and (d) 2348–2352 UTC volume scans. Axes are labeled relative to KOUN. RHI azimuth angle and noteworthy storm features are denoted.

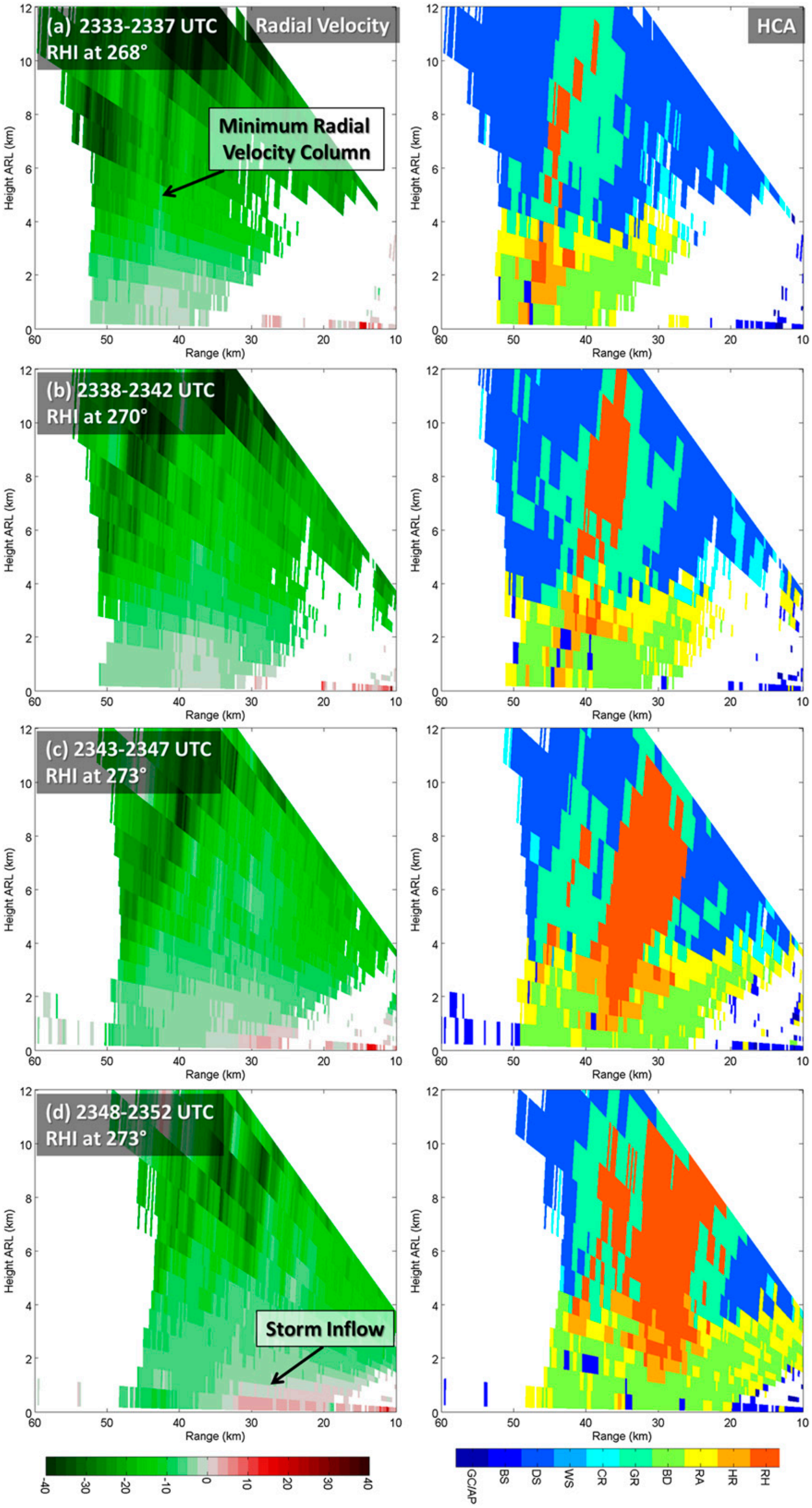

FIG. 7. Reconstructed RHI analyses from KOUN. (left) Radial velocity and (right) HCA are shown at (a) 2333–2337, (b) 2338–2342, (c) 2243–2347, and (d) 2348–2352 UTC volume scans. The classifications used in the right panels are defined in section 2b. Axes are labeled relative to KOUN. RHI azimuth angle and noteworthy storm features are denoted.

particular storm, there was a large area of graupel in the cold-cloud region that was a much greater area than the warm-cloud region, suggesting graupel embryos were the precursor to hail formation. The areal increase of rain and hail mixture aloft from the conversion of graupel was probably due to the intense updraft, as indicated by the persistent, deep Z_{DR} column.

The Z_{DR} column continued to maintain itself in the 2343–2347 UTC volume scan (Fig. 6c). Behind the primary Z_{DR} column, there was evidence of a developing secondary Z_{DR} column ~44 km downrange from the radar. The height of the secondary Z_{DR} column was only ~4.6 km ARL with a Z_{DR} estimate of 2.1 dB at the top of the column. The secondary Z_{DR} column may represent an updraft pulse behind the primary updraft. A secondary region of enhanced radar reflectivity within and above the secondary Z_{DR} column, separated from the primary region of enhanced reflectivity, is further evidence of an updraft pulse. Furthermore, the HCA output (Fig. 7c) also indicates a new region of rain and hail mixture within and above the secondary Z_{DR} column. This updraft pulse represents the multicellular nature of these storms; recall that the storm had previously split into two distinct cells. There also was an increase in outbound radial velocities in the lowest two elevation scans ~(25–32) km downrange from the radar, indicating increased inflow into the storm.

The storm maintained its intensity during the 2348–2352 UTC volume scan (Fig. 6d). The primary Z_{DR} column was still present to ~5.7 km ARL with a Z_{DR} estimate of 1.3 dB at the top of the column. The Z_{DR} column had become offset slightly downrange of the greatest reflectivity estimates. A large area of ≥60-dBZ radar reflectivity was present, primarily from the 0°C level and above. In addition, the outbound radial velocities (Fig. 7d) had expanded even farther downrange and higher into the storm, nearly coincident with the location of the Z_{DR} column. Therefore, the depth and intensity of the inflow into the storm had continued to increase in this volume scan. Evidence of the updraft pulse from the previous volume scan was still present as indicated by a secondary Z_{DR} column, enhanced radar reflectivity, and a separated rain and hail mixture region downrange from the primary Z_{DR} column. The areal coverage of the primary rain and hail mixture had continued to increase aloft during this volume scan as well.

In the next series of volume scans (Figs. 8 and 9), there is evidence of at least one descending reflectivity core to the surface. During the 2358–0002 UTC volume scan, there was an area of ≥60 dBZ, $Z_{\mathrm{DR}} \sim 0$ dB, and a decrease in ρ_{hv} ~ (20–30) km downrange from the radar that had descended to near the surface (Fig. 8b). In the HCA output, there is separated area of rain and hail mixture that has descended to the surface (Fig. 9b). There were no reported wind or hailstones with this descending reflectivity core; however, this is evidence that this storm was capable of producing several downburst and/or hail events as the storm continued to maintain its intensity even after the reflectivity core had descended to the surface. In addition, this series of volume scans indicates that the Z_{DR} column dissipated and reappeared within the storm in subsequent volume scans. However, this was probably an artifact of the WSR-88D's sampling of the storm; frequent and dense midlevel scans are necessary to accurately monitor the Z_{DR} column and associated updraft strength (Snyder et al. 2015; Tanamachi and Heinselman 2016). The reappearance of the Z_{DR} column on the 0008–0012 UTC volume scan (~13 km downrange from the radar) without any weakening of the storm brings credence to this hypothesis (Fig. 8d). The Z_{DR} column is nearly collocated with low-level radial convergence and a bounded weak-echo region (BWER), which is further evidence this is the location of the updraft. The HCA indicates big drops within the BWER, which would be expected since these are oblate hydrometeors (e.g., Kumjian and Ryzhkov 2008; Kumjian et al. 2012). Unfortunately, because of the radar cone of silence, the radar is only able to see below the 0°C level in the region.

The next three volume scans capture the microphysical evolution of the Norman downburst (Figs. 10 and 11). A rain and hail core aloft was present ~(5–8) km downrange from the radar during the 0013–0017 UTC volume scan (Fig. 10a). The HCA output indicates the presence of rain and hail mixture within this region (Fig. 11a). Although the rain and hail mixture does not have a clear boundary downrange on the HCA output, increased Z_{DR} estimates on either side of the rain and hail core can be utilized to separate out a distinct rain and hail core. The rain and hail core was located as low as ~0.6 km ARL; the top of the rain and hail core was not sampled because of the radar cone of silence. The radar sampled radar reflectivity ≥60 dBZ, $Z_{\mathrm{DR}} \sim 0$ dB, and a decrease in ρ_{hv} within the rain and hail core. Outbound velocities became inbound ~11 km downrange from the radar, indicating the presence of low-level radial convergence (~500-m depth), likely associated with the updraft. Evidence of an updraft is suggested by a Z_{DR} column and BWER located above the region of low-level radial convergence. Recall the 1-min mesonet observations had measured a minimum atmospheric pressure at 0013 UTC (Fig. 4). This is further evidence that the pressure minimum may have been dynamically induced by converging and rising air into the updraft ahead of the gust front.

The rain and hail core began to rapidly descend during the 0018–0022 UTC volume scan (Fig. 10b). The HCA output indicates the rain and hail mixture at the lowest

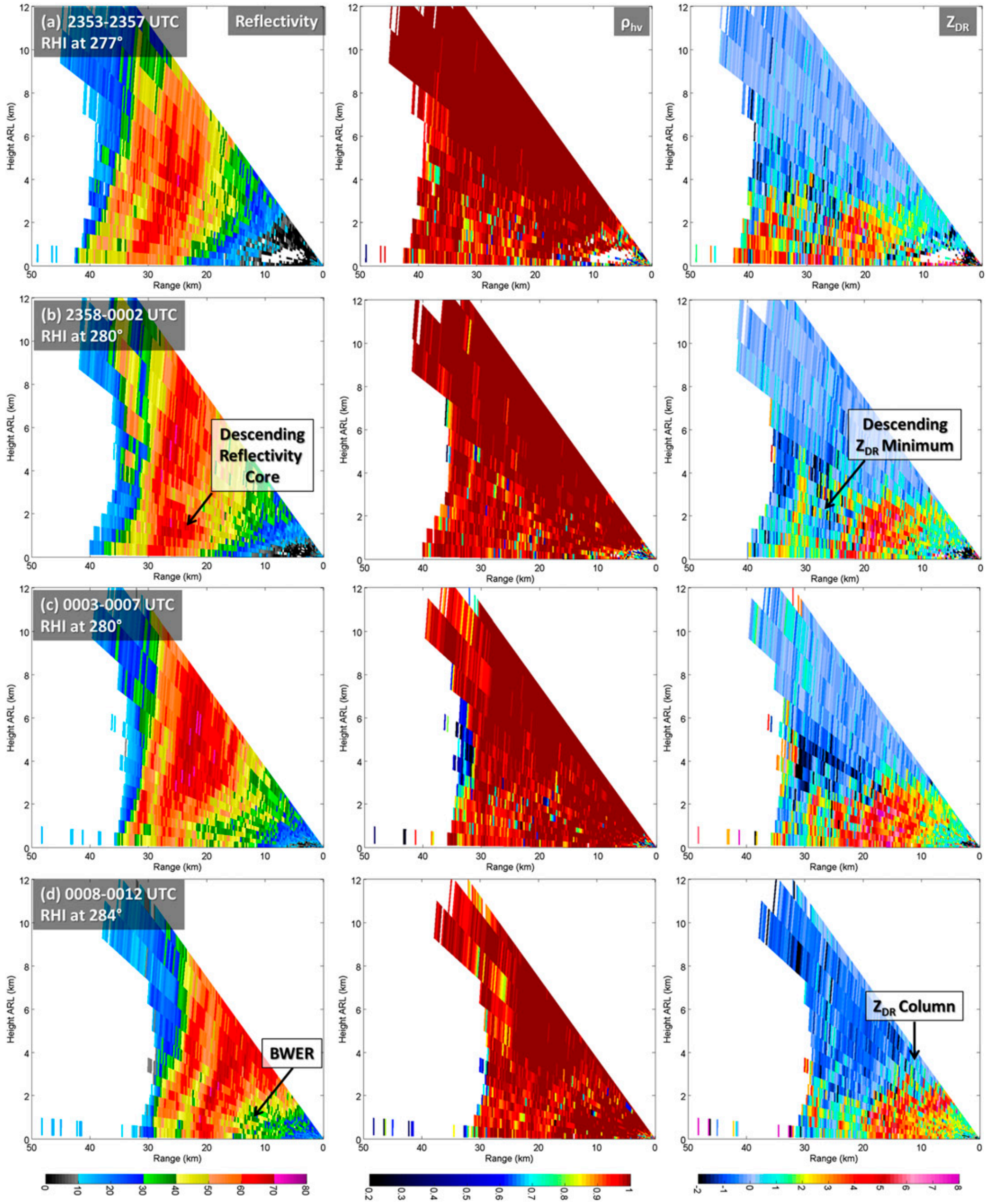

FIG. 8. As in Fig. 6, but at (a) 2353–2357, (b) 2358–0002, (c) 0003–0007, and (d) 0008–0012 UTC volume scans.

elevation scan ~6 km downrange from the radar, which is only ~55 m ARL (Fig. 11b). During the rain and hail core's descent, Z_{DR} increased and ρ_{hv} decreased on the bottom periphery of the rain and hail core. The increased Z_{DR} and decreased ρ_{hv} are assumed to be due to the increasing presence of water coating on the descending hailstones. Therefore, it is surmised that there was hail melting in the lower part of the rain and hail core through the combined use of the HCA output and the dual-pol radar estimates. Also, there was an area of radial divergence immediately below and within the descending hail core at ~0.4 km ARL. The area of radial divergence was somewhat broad, with near-zero radial velocities in the center. The near-zero radial velocities centered within broad divergence implies the flow was more vertical rather than horizontal within this portion of the storm, probably because of the descending downburst. There was still an inflow region, albeit shallower, present in this volume scan. This inflow region was immediately below the region of broad radial

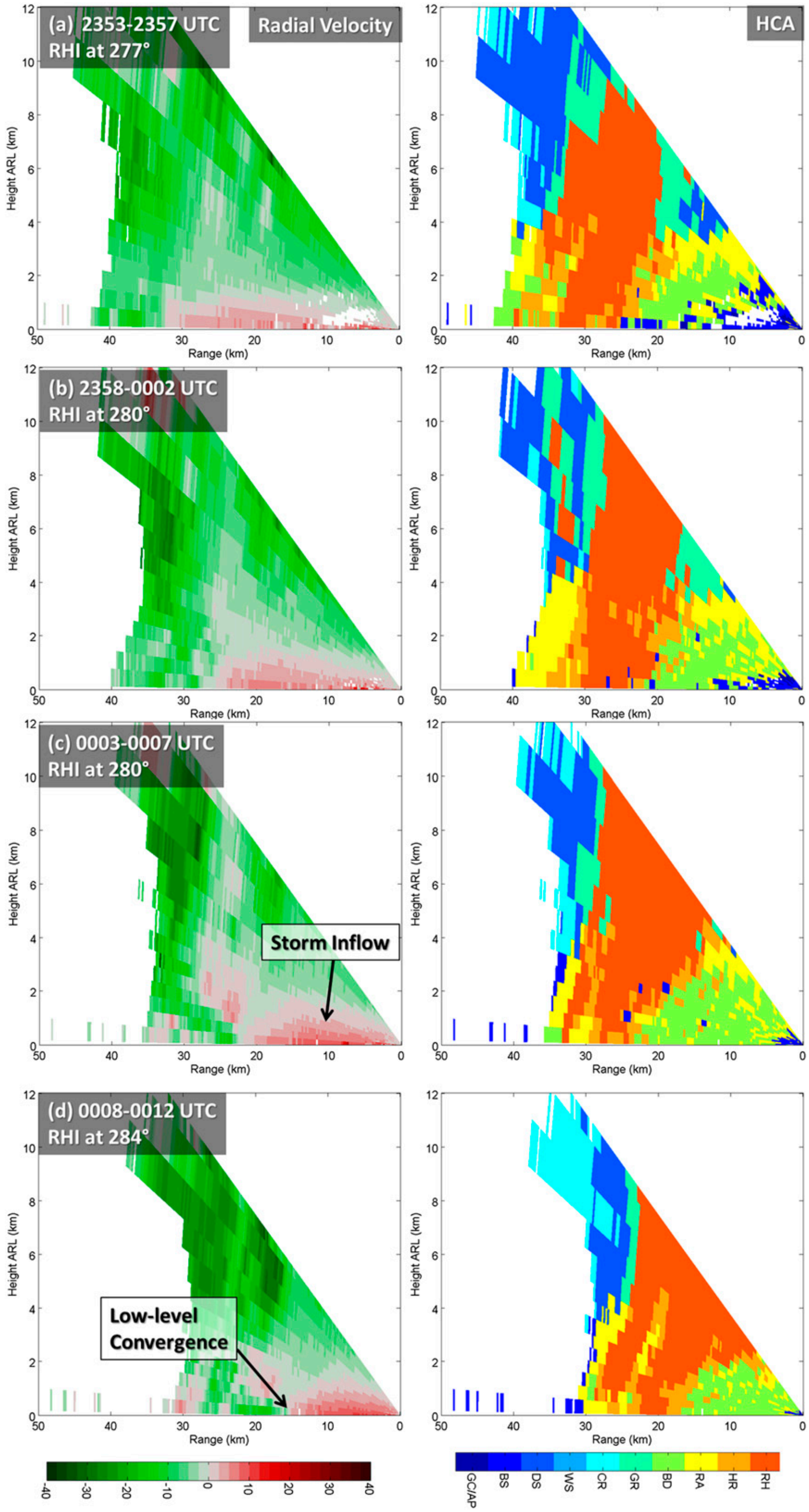

FIG. 9. As in Fig. 7, but at (a) 2353–2357, (b) 2358–0002, (c) 0003–0007, and (d) 0008–0012 UTC volume scans.

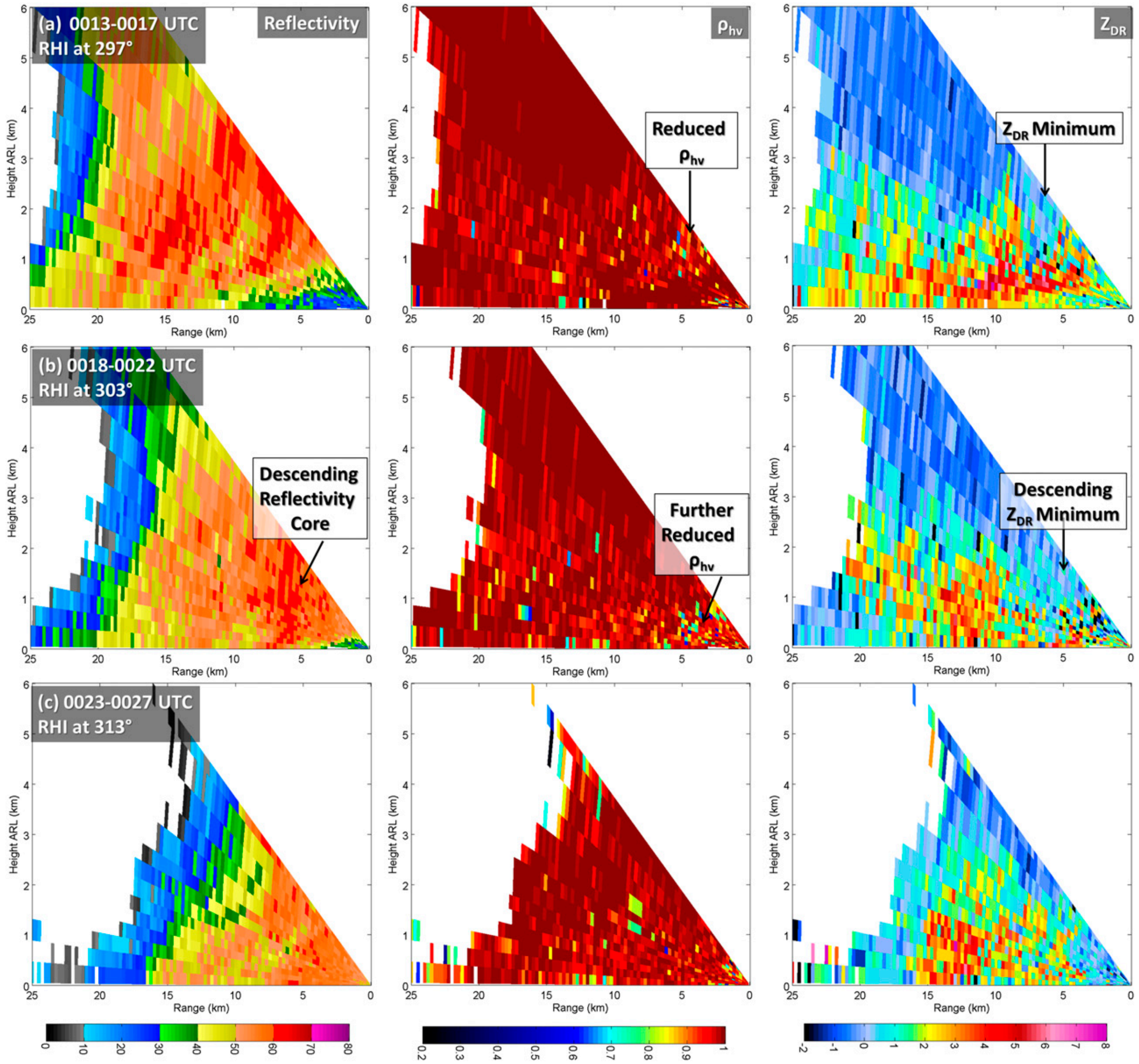

FIG. 10. As in Fig. 6, but at (a) 0013–0017, (b) 0018–0022, and (c) 0023–0027 UTC volume scans.

divergence, indicating the downburst had not made it to the surface. The HCA output indicates there was a shallow zone of heavy rain, big drops, and rain immediately below the rain and hail mixture region. The outbound radial velocities had decreased to a maximum estimate of $9\,\mathrm{m\,s^{-1}}$, implying a decrease in inflow into the storm. This is coincident with a disappearance of the Z_{DR} column from the previous volume scan. The implication of the weakening inflow and the disappearance of the Z_{DR} column is the storm may have become more downdraft rather than updraft dominant.

The downburst was ongoing by the 0023–0027 volume scan (Fig. 10c). Note the change in radial convergence at low-levels to radial divergence from the previous volume scan (Fig. 11c). This indicates that the updraft at these lower levels had turned into a downdraft. The maximum inbound radial velocity was $33\,\mathrm{m\,s^{-1}}$. Recall the 1-min mesonet observations (which were nearly collocated with the radar) had detected passage of the gust front at 0025 UTC, which was followed by a peak wind gust of $31.5\,\mathrm{m\,s^{-1}}$ at 0029 UTC (Fig. 4). A slight time lag in the surface observations is expected because the downburst began ~5 km downrange (i.e., upstream) from the radar. The HCA output indicates the rain and hail mixture had descended in the immediate vicinity of the radar, implying that the descent of the rain and hail core aloft was coincident with downburst.

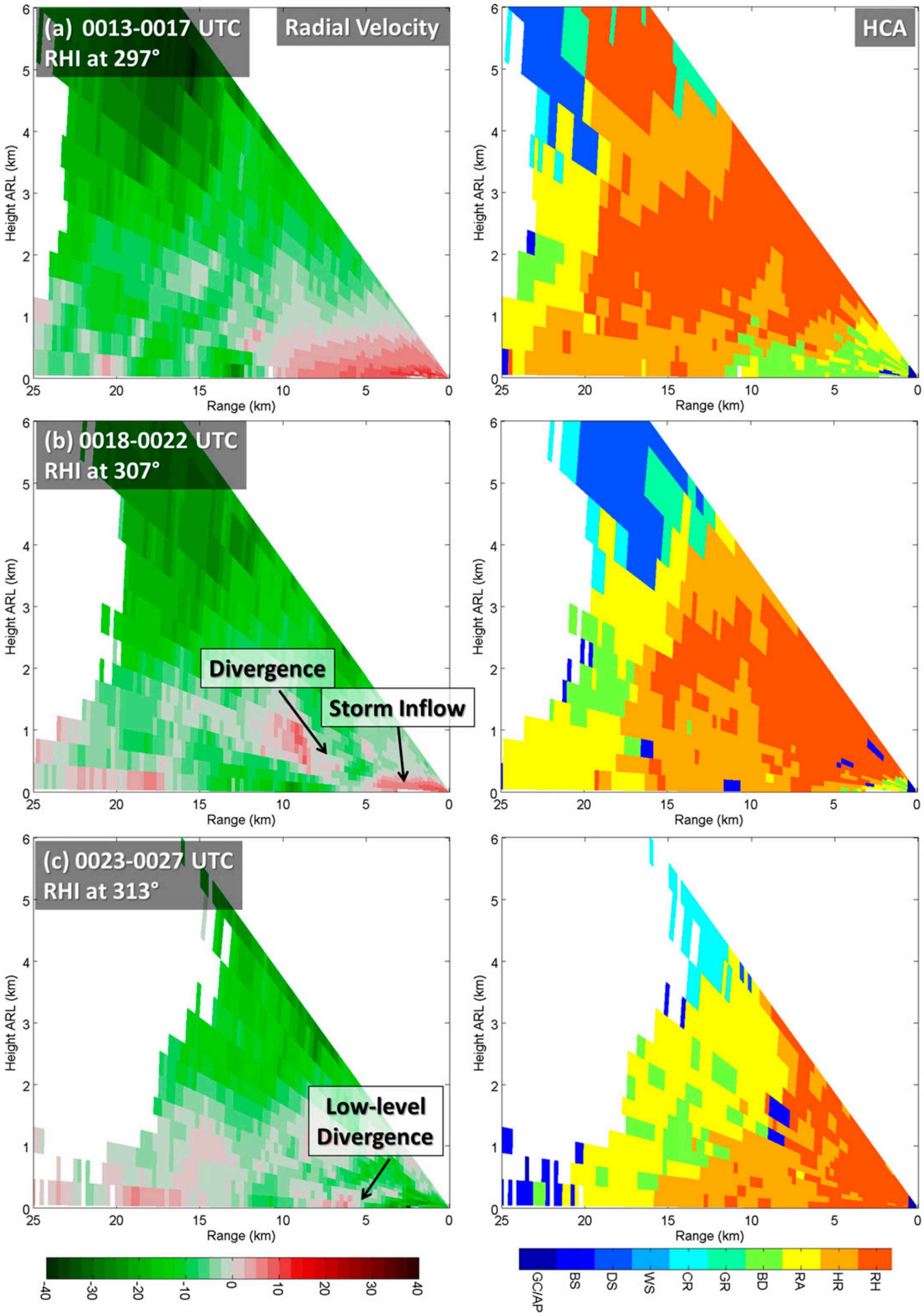

FIG. 11. As in Fig. 7, but at (a) 0013–0017, (b) 0018–0022, and (c) 0023–0027 UTC volume scans.

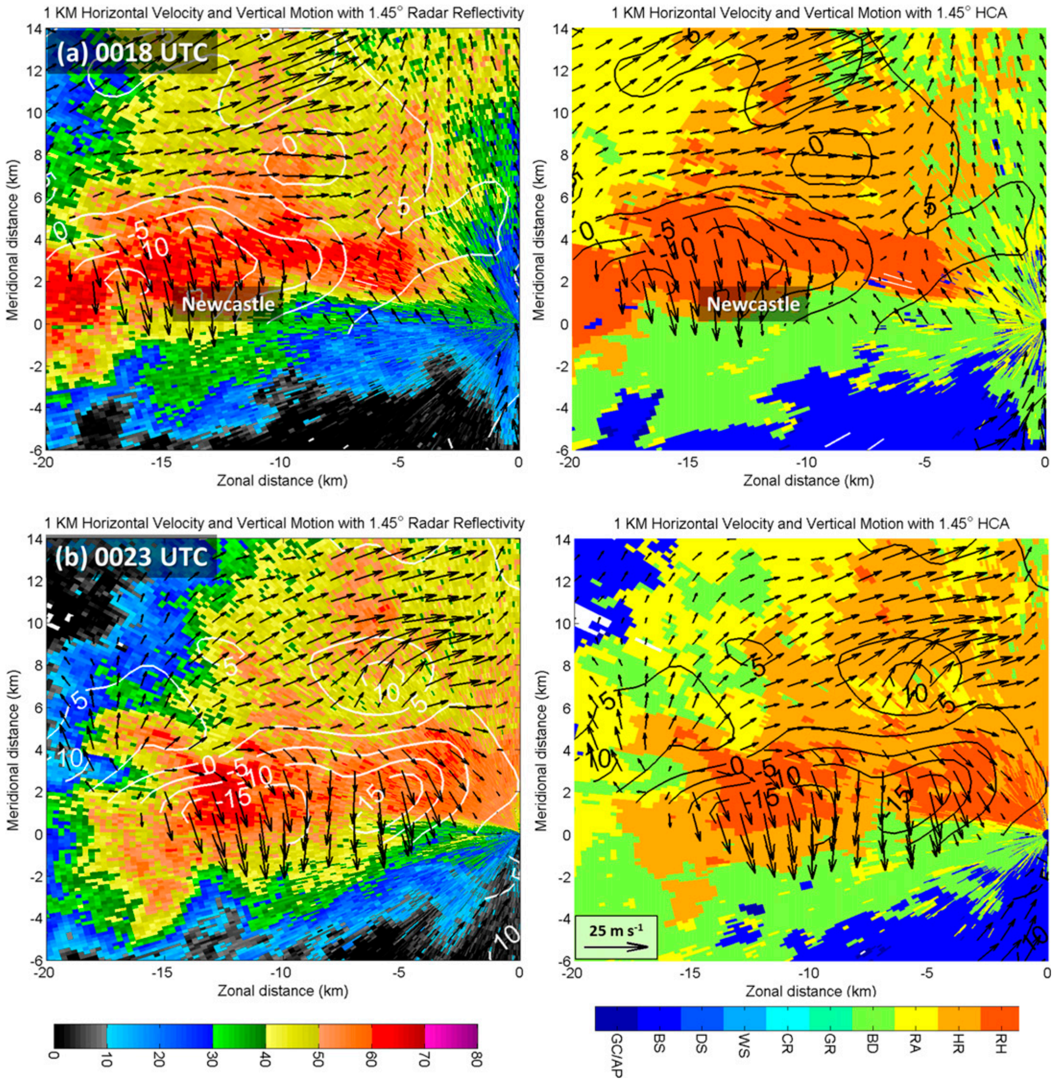

FIG. 12. Dual-Doppler analysis at (a) 0018 and (b) 0023 UTC with KOUN 1.45° radar reflectivity and HCA. Dual-Doppler analysis includes horizontal velocity vectors and vertical velocity contours. Contours are plotted in 5 m s^{-1} intervals in white on the radar reflectivity panels and in black on the HCA panels. The location of Newcastle is indicated in (a).

Dual-Doppler analyses were conducted on the radar data using both KOUN and KTLX WSR-88Ds; however, because of the beam-crossing angle, only two volume scans could be analyzed. KTLX is located approximately 20 km to the northeast of KOUN. At the time of the event, KTLX was not upgraded to have dual-pol capabilities. The radar data were transformed from the radar coordinate system into a Cartesian coordinate system using the National Center for Atmospheric Research (NCAR) "REORDER" objective analysis software package (Oye and Case 1995). Once the objective analysis was complete, dual-Doppler analysis was done using NCAR's Custom Editing and Display of Reduced Information in Cartesian Space (CEDRIC) software package, which conducts its dual-Doppler analysis by finding the projection of the particle motion along the Doppler radar radial direction (Miller and Fredrick 1998). A simple advection correction, using the mean storm motion, was implemented to center the radar data at the 0018 and 0023 for the two dual-Doppler analyses. The 1 km above sea level (MSL) horizontal wind vectors and vertical velocity are overlaid on the 1.45° radar scans and the HCA output in Fig. 12.

The analysis at 0018 UTC (Fig. 12a) indicates an elongated storm structure. A minimum vertical velocity of ~-17 m s^{-1} was present ~17 km west of the radar. There were wind reports from this storm prior to the reports in Norman. Approximately 3 km southwest of

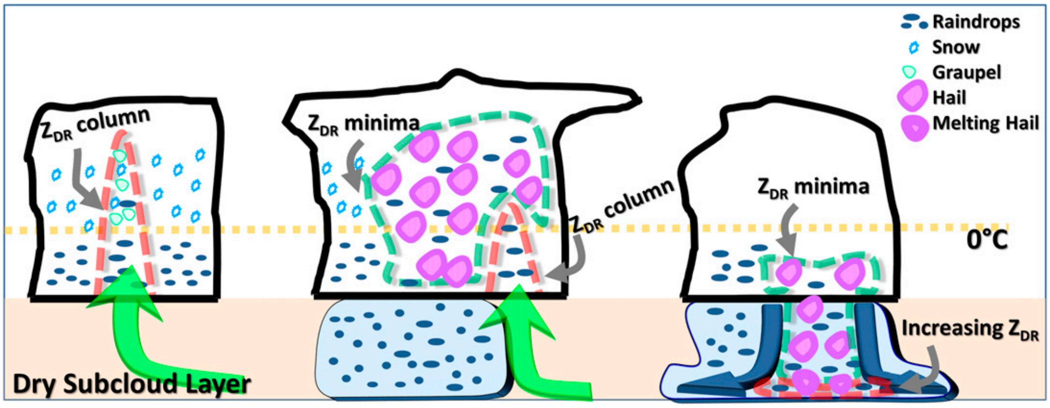

FIG. 13. Schematics of the microphysical evolution of hydrometeors during the Norman downburst as observed by PRD and the applied HCA. The schematics depict raindrops, snow, graupel, hail, and melting hail. Increasing water coating on the melting hailstones is depicted by the increasing line width of the hailstones. The 0°C level is depicted by the dotted horizontal yellow line. Local Z_{DR} maxima (i.e., Z_{DR} columns) are depicted by the dashed red line. Local Z_{DR} minima are depicted by the dashed green line. The updraft and downburst locations are depicted by the green and blue arrows, respectively. The shaded blue region represents the cold pool. It is assumed that diabatic cooling from hail melting and rain evaporation plays an important role in accelerating the downdraft to result in a downburst.

Newcastle, Oklahoma, there were reports of 31–35 m s^{-1} wind gusts between 0020 and 0023 UTC. Along with the wind gusts, 2.5-cm hailstones were reported as well. Recall there was evidence in the RHI analyses of a possible descending rain and hail core separate from the Norman downburst (Fig. 8d). The dual-Doppler analysis provides further evidence that this storm was capable of multiple downbursts. The multicellular structure is more evident in the 0023 UTC analysis (Fig. 12b). Note the presence of two distinct hail cores with separate vertical motion minima approximately 8 km apart. The development of a multicellular structure was previously noted in the polarimetric observations of two distinct Z_{DR} columns (Figs. 8a,b). There was a divergent wind pattern, which is expected near the surface in a downburst. In addition, there was very strong downward motion with a minimum vertical velocity of ~ -20 m s^{-1}, which has been previously used to define downbursts (Srivastava 1985). Much of the downward motion in the dual-Doppler analysis was collocated in the rain and hail mixture, which is further confirmation of the wet downburst by radar observations.

Figure 13 describes the evolution of the microphysics associated with the downburst. Overall, in the early stages of the convective storm (as it was splitting), an area of graupel was developing within the updraft of the storm (Fig. 7a). This updraft was detected by the presence of a Z_{DR} column (Fig. 6a). The greatest expansion of graupel aloft occurred in early stages of the storm. The large area of graupel was in the cold-cloud region, suggesting graupel embryos were the precursor to hail formation. The area of graupel began to convert to a rain and hail mixture (Figs. 7b–d). The areal increase of rain and hail mixture aloft from the conversion of graupel was probably due to the intense updraft, as indicated by the persistent, deep Z_{DR} column that had penetrated the 0°C level (Figs. 6a–c). The rain and hail mixture continued to expand significantly above the 0°C level. Eventually the majority of the graupel evolved into a mixture of mostly rain and hail (Fig. 9). After continued areal expansion, the area of rain and hail mixture eventually descended to the ground. Evidence of the hail core's descent began as early as the 0003–0007 UTC volume scan, nearly 20–30 min before there are significant impacts from the downburst (Figs. 9c,d); however, the most significant descent occurred after the 0013–0017 UTC volume scan (Figs. 11a,b). As it descended to the ground, radial divergence developed immediately below and within the descending hail core (Fig. 11b). In addition, evidence of Z_{DR} column (i.e., the updraft) had dissipated (Fig. 10b). Eventually, the downburst reached the surface, as indicated by radial convergence becoming radial divergence on the lowest elevation scan (Fig. 11c).

Studies have shown that ice hydrometeors (i.e., hailstones) can play a significant role in downbursts by increasing the intensity of the downdraft relative to just rain (e.g., Srivastava 1987; Atkins and Wakimoto 1991; Fu and Guo 2007). Fu and Guo (2007) found in their simulated downburst that hail-loading, melting hailstones, and evaporation of rain were crucial in the formation of downbursts within their storm. This observational study on the evolution of hydrometeors and the inferred phase changes using polarimetric radar data support the importance of these processes in wet downburst formation.

Also noted earlier, the atmosphere was highly conducive for downbursts on this day. Recall that the environmental lapse rate was nearly dry adiabatic in the subcloud layer (Fig. 1). For wet downbursts, as the environmental lapse rate increases, lower water content is needed for a downburst (Srivastava 1985); the deep, dry adiabatic layer was probably even sufficient to produce dry downbursts on this day (Srivastava 1985; Proctor 1989; Wakimoto et al. 1994). The intense rain rate ($213\,\mathrm{mm\,h^{-1}}$) and the large rain and hail mixture aloft indicate that the storm had relatively high water content. Srivastava (1985) found if the environmental lapse rate is dry adiabatic, the greater the rainfall rate (or reflectivity), the more intense the downburst. Therefore, it can be surmised that an observed rapid growth of an expansive rain and hail mixture, as can be revealed by dual-pol data, would indicate imminent risk of a downburst on a day with similar thermodynamic conditions. Note that this was still ~30 min before the downburst caused damage at the surface; therefore, closely monitoring polarimetric radar data and real-time HCA output can help forecast and warning of strong downbursts in a real-time operational setting.

5. Conclusions

A thunderstorm that initiated ahead of a cold front split off and produced a significant downburst approximately within an hour time scale. Here is a summary of the significant findings from this study:

- Polarimetric radar estimates indicated the presence of a strong updraft, as indicated by a persistent, deep Z_{DR} column that had penetrated the 0°C level. The primary Z_{DR} column had dissipated as the downburst occurred. A secondary Z_{DR} column indicated the presence of a secondary updraft pulse within the multicellular thunderstorm.
- During the early stage, an area of mostly graupel and some rain and hail mix expanded aloft. Eventually, the graupel evolved to nearly all rain and hail mixture above the 0°C level. This large area of rain and hail mixture descended to the ground during the downburst. Increased Z_{DR} and decreased ρ_{hv} at the bottom of the rain and hail mixture are assumed to be due to the increasing presence of water coating on the descending hailstones.
- One-min surface observations from the Oklahoma Mesonet indicated a 6.6-hPa pressure rise that was coincident with a rain rate of $213\,\mathrm{mm\,h^{-1}}$ at the center of the downburst. The maximum atmospheric pressure being coincident with the peak rain rate indicates precipitation loading was a cause of this wet downburst. The 1-min observations also indicated the presence of multiple downburst surges and were linked to radar observations through the locations of the updraft and downdraft within the storm.
- Dual-Doppler analysis indicates intense downward motion with a minimum vertical velocity of $\sim -20\,\mathrm{m\,s^{-1}}$. This downward motion was coincident with rain and hail mixture, which is further confirmation of the wet downburst through radar observations.

This study shows the important roles polarimetric radars can play in microphysical studies, in particular microphysical processes associated with an intense downburst event. Without the polarimetric observations, it is difficult to determine the dominant hydrometeor types or infer related microphysics processes or updraft strength. With the help of an HCA that depends on polarimetric radar information, the spatial distributions of microphysical species and their time evolution can be estimated, and the associated microphysical processes inferred. The information from the polarimetric radar estimates, combined with dual-Doppler wind retrieval, was able to depict clearly the time evolution of the developing downburst, and its surface winds and thermodynamic features are captured well by mesonet station measurements at 1-min intervals. It was also shown that important precursors (i.e., rapid hail growth aloft) of the developing downburst was evident with up to 30-min lead time before surface wind gust, suggesting important values of polarimetric radar data for nowcasting and warning of severe downburst events. This especially is important when the environment is very favorable for downbursts.

This study complements a very recent analysis conducted by Kuster et al. (2016). Kuster et al. (2016) focused on resolving downburst precursors through the use of KOUN and 1-min PAR data. In their study, they calculated and evaluated the temporal evolution of midlevel radial convergence and descending reflectivity cores. They found in severe downbursts that midlevel convergence increased to a maximum value and then decreased as the reflectivity core descended. Both studies note the descending Z_{DR} minimum associated with the downburst. However, this study provided additional information about the microphysics by incorporating the use of ρ_{hv} (in addition to Z_{DR}) and applying an HCA to the dual-pol radar data. As a result, a conceptual model that characterizes the hydrometeor evolution of the parent downburst storm was developed (Fig. 13). In addition, this study provided an in-depth analysis of 1-min mesonet station data at the location of the downburst (Figs. 3 and 4).

Being a study mainly based on observational data, many aspects of this study have to remain qualitative. The eventual goal is to perform modeling studies with this case, with carefully designed sensitivity experiments to further study the microphysical processes and their interactions with the storms and the environment, and to use the observational information to cross validate the modeling results.

Acknowledgments. This work was supported by National Science Foundation (NSF) Grant AGS-1046171. The third author was also supported by NSF Grants AGS-0802888 and AGS-1261776. The authors thank Drs. Matthew Bunkers and James Kurdzo and the two anonymous reviewers who provided constructive feedback on the original version of this paper. The authors also acknowledge the National Severe Storms Laboratory for providing KOUN WSR-88D data and the Oklahoma Climatological Survey for providing the Oklahoma Mesonet 1-min data.

REFERENCES

Atkins, N. T., and R. M. Wakimoto, 1991: Wet microburst activity over the southeastern United States: Implications for forecasting. *Wea. Forecasting*, **6**, 470–482, doi:10.1175/1520-0434(1991)006<0470:WMAOTS>2.0.CO;2.

Atlas, D., C. W. Ulbrich, and C. R. Williams, 2004: Physical origin of a wet microburst: Observations and theory. *J. Atmos. Sci.*, **61**, 1186–1195, doi:10.1175/1520-0469(2004)061<1186:POOAWM>2.0.CO;2.

Brandes, E. A., and K. Ikeda, 2004: Freezing-level estimation with polarimetric radar. *J. Appl. Meteor.*, **43**, 1541–1553, doi:10.1175/JAM2155.1.

Brock, F. V., K. C. Crawford, R. L. Elliott, G. W. Cuperus, S. J. Stadler, H. L. Johnson, and M. D. Eilts, 1995: The Oklahoma Mesonet: A technical overview. *J. Atmos. Oceanic Technol.*, **12**, 5–19, doi:10.1175/1520-0426(1995)012<0005:TOMATO>2.0.CO;2.

Emanuel, K. A., 1994: *Atmospheric Convection*. Oxford University Press, 580 pp.

Evans, J., and D. Turnbull, 1989: Development of an automated windshear detection system using Doppler weather radar. *Proc. IEEE*, **77**, 1661–1673, doi:10.1109/5.47729.

Fu, D., and X. Guo, 2007: Numerical study on a severe downburst-producing thunderstorm on 23 August 2001 in Beijing. *Adv. Atmos. Sci.*, **24**, 227–238, doi:10.1007/s00376-007-0227-2.

Fujita, T. T., 1985: The downburst, microburst and macroburst. SMRP Rep. 210, 122 pp. [NTIS PB-85-148880.]

——, 1986: DFW microburst on August 2, 1985. SMRP Rep. 217, 154 pp. [NTIS PB-86-131638.]

——, and F. Caracena, 1977: An analysis of three weather-related aircraft accidents. *Bull. Amer. Meteor. Soc.*, **58**, 1164–1181, doi:10.1175/1520-0477(1977)058<1164:AAOTWR>2.0.CO;2.

Giangrande, S. E., J. M. Krause, and A. V. Ryzhkov, 2008: Automatic designation of the melting layer with a polarimetric prototype of the WSR-88D radar. *J. Appl. Meteor. Climatol.*, **47**, 1354–1364, doi:10.1175/2007JAMC1634.1.

Glickman, T., Ed., 2000: *Glossary of Meteorology*. 2nd ed. Amer. Meteor. Soc., 855 pp. [Available online at http://glossary.ametsoc.org/.]

Hall, M. P. M., J. W. F. Goddard, and S. M. Cherry, 1984: Identification of hydrometeors and other targets by dual-polarization radar. *Radio Sci.*, **19**, 132–140, doi:10.1029/RS019i001p00132.

Harimaya, T., 1976: The embryo and formation of graupel. *J. Meteor. Soc. Japan Ser. II*, **54**, 42–51. [Available online at https://www.jstage.jst.go.jp/article/jmsj1965/54/1/54_1_42/_pdf.]

Knight, N. C., 1981: The climatology of hailstone embryos. *J. Appl. Meteor.*, **20**, 750–755, doi:10.1175/1520-0450(1981)020<0750:TCOHE>2.0.CO;2.

Kosiba, K., J. Wurman, Y. Richardson, P. Markowski, P. Robinson, and J. Marquis, 2013: Genesis of the Goshen County, Wyoming, tornado on 5 June 2009 during VORTEX2. *Mon. Wea. Rev.*, **141**, 1157–1181, doi:10.1175/MWR-D-12-00056.1.

Kumjian, M. R., and A. V. Ryzhkov, 2008: Polarimetric signatures in supercell thunderstorms. *J. Appl. Meteor. Climatol.*, **47**, 1940–1961, doi:10.1175/2007JAMC1874.1.

——, S. M. Ganson, and A. V. Ryzhkov, 2012: Freezing of raindrops in deep convective updrafts: A microphysical and polarimetric model. *J. Atmos. Sci.*, **69**, 3471–3490, doi:10.1175/JAS-D-12-067.1.

Kuster, C. M., P. L. Heinselman, and T. J. Schuur, 2016: Rapid-update radar observations of downbursts occurring within an intense multicell thunderstorm on 14 June 2011. *Wea. Forecasting*, **31**, 827–851, doi:10.1175/WAF-D-15-0081.1.

Lamb, D., and J. Verlinde, 2011: *Physics and Chemistry of Clouds.* Cambridge University Press, 584 pp.

Lim, S., V. Chandrasekar, and V. N. Bringi, 2005: Hydrometeor classification system using dual-polarization radar measurements: Model improvements and in situ verification. *IEEE Trans. Geosci. Remote Sens.*, **43**, 792–801, doi:10.1109/TGRS.2004.843077.

Liu, H., and V. Chandrasekar, 2000: Classification of hydrometeors based on polarimetric radar measurements: Development of fuzzy logic and neuro-fuzzy systems, and in situ verification. *J. Atmos. Oceanic Technol.*, **17**, 140–164, doi:10.1175/1520-0426(2000)017<0140:COHBOP>2.0.CO;2.

Loney, M. L., D. S. Zrnić, J. M. Straka, and A. V. Ryzhkov, 2002: Enhanced polarimetric radar signatures above the melting level in a supercell storm. *J. Appl. Meteor.*, **41**, 1179–1194, doi:10.1175/1520-0450(2002)041<1179:EPRSAT>2.0.CO;2.

Mahale, V. N., G. Zhang, and M. Xue, 2013: The microphysics of the 14 June 2011 Norman, Oklahoma, downburst from dual-polarization and dual-Doppler radar measurements. *16th Conf. on Aviation, Range, and Aerospace Meteorology*, Austin, TX, Amer. Meteor. Soc., 5.1. [Available online at https://ams.confex.com/ams/93Annual/webprogram/Manuscript/Paper216605/Microphysics_14_June_2011_Downburst_Mahale_Zhang_Xue.pdf.]

——, ——, and ——, 2014: Fuzzy logic classification of S-band polarimetric radar echoes to identify three-body scattering and improve data quality. *J. Appl. Meteor. Climatol.*, **53**, 2017–2033, doi:10.1175/JAMC-D-13-0358.1.

Marquis, J., Y. Richardson, J. Wurman, and P. Markowski, 2008: Single- and dual-Doppler analysis of a tornadic vortex and surrounding storm-scale flow in the Crowell, Texas, supercell of 30 April 2000. *Mon. Wea. Rev.*, **136**, 5017–5043, doi:10.1175/2008MWR2442.1.

McCann, D. W., 1994: WINDEX—A new index for forecasting microburst potential. *Wea. Forecasting*, **9**, 532–541, doi:10.1175/1520-0434(1994)009<0532:WNIFFM>2.0.CO;2.

McPherson, R. A., and Coauthors, 2007: Statewide monitoring of the mesoscale environment: A technical update on the Oklahoma Mesonet. *J. Atmos. Oceanic Technol.*, **24**, 301–321, doi:10.1175/JTECH1976.1.

Melnikov, V. M., and D. S. Zrnić, 2007: Autocorrelation and cross-correlation estimators of polarimetric variables. *J. Atmos. Oceanic Technol.*, **24**, 1337–1350, doi:10.1175/JTECH2054.1.

Merritt, M. W., D. Klingle-Wilson, and S. D. Campbell, 1989: Wind shear detection with pencil-beam radars. *Lincoln Laboratory Journal*, Vol. 2, MIT, 483–510. [Available online at https://www.ll.mit.edu/publications/journal/pdf/vol02_no3/2.3.10.windshearpencilradar.pdf.]

Miller, L. J., and S. M. Fredrick, 1998: CEDRIC: Custom Editing and Display of Reduced Information in Cartesian Space. National Center for Atmospheric Research Tech. Manual, 130 pp. [Available online at http://www.eol.ucar.edu/system/files/cedric_doc.pdf.]

Morris, D. A., and M. A. Shafer, 1996: Detailed surface observations during the Lahoma hail and windstorm. Preprints, *18th Conf. on Severe Local Storms*, San Francisco, CA, Amer. Meteor. Soc., 65–69.

National Transportation Safety Board, 1983: Aircraft accident report: Pan American World Airways, Inc., Clipper 759, Boeing 727-235, N4737, New Orleans International Airport Kenner, Louisiana July 9, 1982. NTSB Rep. AAR-83-02, 113 pp. [NTIS PB 83-910402.] [Available online at http://www.ntsb.gov/investigations/AccidentReports/Reports/AAR8302.pdf.]

NOAA/NCDC, 2011a: NEXRAD Level-II radar data. NOAA/NCDC, accessed 20 April 2012. [Available online at https://www.ncdc.noaa.gov/data-access/radar-data/nexrad.]

——, 2011b: Storm events database. NOAA/NCDC, accessed 2 August 2015. [Available online at http://www.ncdc.noaa.gov/stormevents.]

NWS, 2014: Weather Forecast Office severe weather products specification. NWS Rep. 10–511, 35 pp. [Available online at http://www.nws.noaa.gov/directives/sym/pd01005011curr.pdf.]

Office of the Federal Coordinator for Meteorological Services and Supporting Research, 2011: Doppler radar meteorological observations. Part A: System concepts, responsibilities, and procedures. Federal Meteorological Handbook 11, FCM-H11A-2011. [Available online at http://www.roc.noaa.gov/wsr88d/PublicDocs/PartA_FMH11_Rev11.pdf.]

Oklahoma Climatological Survey, 2011: Oklahoma Mesonet surface observation data. University of Oklahoma, accessed 27 January 2015. [Available online at https://www.mesonet.org/index.php/site/contact.]

Oye, D., and M. Case, 1995: REORDER—A program for gridding radar data: Installation and use manual for the UNIX version. National Center for Atmospheric Research Tech. Manual, 44 pp. [Available online at https://www.eol.ucar.edu/system/files/unixreorder.pdf.]

Park, H. S., A. V. Ryzhkov, D. S. Zrnić, and K.-E. Kim, 2009: The hydrometeor classification algorithm for the polarimetric WSR-88D: Description and application to an MCS. *Wea. Forecasting*, **24**, 730–748, doi:10.1175/2008WAF2222205.1.

Proctor, F. H., 1988: Numerical simulations of an isolated microburst. Part I: Dynamics and structure. *J. Atmos. Sci.*, **45**, 3137–3160, doi:10.1175/1520-0469(1988)045<3137:NSOAIM>2.0.CO;2.

——, 1989: Numerical simulations of an isolated microburst. Part II: Sensitivity experiments. *J. Atmos. Sci.*, **46**, 2143–2165, doi:10.1175/1520-0469(1989)046<2143:NSOAIM>2.0.CO;2.

Pruppacher, H. R., and J. D. Klett, 1997: *Microphysics of Clouds and Precipitation.* 2nd ed. Kluwer, 954 pp.

Richter, H., J. Peter, and S. Collis, 2014: Analysis of a destructive wind storm on 16 November 2008 in Brisbane, Australia. *Mon. Wea. Rev.*, **142**, 3038–3060, doi:10.1175/MWR-D-13-00405.1.

Saxion, D. S., and R. L. Ice, 2012: New science for the WSR-88D: Status of the dual-polarization upgrade. *28th Conf. on Interactive Information Processing Systems*, New Orleans, LA, Amer. Meteor. Soc., 5. [Available online at https://ams.confex.com/ams/92Annual/webprogram/Manuscript/Paper197645/NEXRAD_DP_Status_28th_IIPS_Jan2012.pdf.]

Scharfenberg, K. A., 2003: Polarimetric radar signatures in microburst-producing thunderstorms. *31st Int. Conf. on Radar Meteorology*, Seattle, WA, Amer. Meteor. Soc., 8B.4. [Available online at https://ams.confex.com/ams/pdfpapers/64413.pdf.]

Skinner, P. S., C. C. Weiss, J. L. Schroeder, L. J. Wicker, and M. I. Biggerstaff, 2011: Observations of the surface boundary structure within the 23 May 2007 Perryton, Texas, supercell. *Mon. Wea. Rev.*, **139**, 3730–3749, doi:10.1175/MWR-D-10-05078.1.

Snyder, J. C., A. V. Ryzhkov, M. R. Kumjian, A. P. Khain, and J. Picca, 2015: A Z_{DR} column detection algorithm to examine convective storm updrafts. *Wea. Forecasting*, **30**, 1819–1844, doi:10.1175/WAF-D-15-0068.1.

Srivastava, R. C., 1985: A simple model of evaporatively driven downdraft: Application to microburst downdraft. *J. Atmos. Sci.*, **42**, 1004–1023, doi:10.1175/1520-0469(1985)042<1004:ASMOED>2.0.CO;2.

——, 1987: A model of intense downdrafts driven by the melting and evaporation of precipitation. *J. Atmos. Sci.*, **44**, 1752–1773, doi:10.1175/1520-0469(1987)044<1752:AMOIDD>2.0.CO;2.

Straka, J. M., and D. S. Zrnić, 1993: An algorithm to deduce hydrometeor types and contents from multi-parameter radar data. Preprints, *26th Int. Conf. on Radar Meteorology*, Norman, OK, Amer. Meteor. Soc., 513–515.

——, ——, and A. V. Ryzhkov, 2000: Bulk hydrometeor classification and quantification using polarimetric radar data: Synthesis of relations. *J. Appl. Meteor.*, **39**, 1341–1372, doi:10.1175/1520-0450(2000)039<1341:BHCAQU>2.0.CO;2.

Suzuki, S.-I., T. Maesaka, K. Iwanami, R. Misumi, S. Shimizu, and M. Maki, 2010: Multi-parameter radar observation of a downburst storm in Tokyo on 12 July 2008. *SOLA*, **6**, 53–56, doi:10.2151/sola.2010-014.

Tanamachi, R. L., and P. L. Heinselman, 2016: Rapid-scan, polarimetric observations of central Oklahoma severe storms on 31 May 2013. *Wea. Forecasting*, **31**, 19–42, doi:10.1175/WAF-D-15-0111.1.

Vivekanandan, J., S. M. Ellis, R. Oye, D. S. Zrnić, A. V. Ryzhkov, and J. Straka, 1999: Cloud microphysics retrieval using S-band dual-polarization radar measurements. *Bull. Amer. Meteor. Soc.*, **80**, 381–388, doi:10.1175/1520-0477(1999)080<0381:CMRUSB>2.0.CO;2.

Wakimoto, R. M., 2001: Convectively driven high wind events. *Severe Convective Storms*, *Meteor. Monogr.*, No. 50, Amer. Meteor. Soc., 255–298.

——, and V. N. Bringi, 1988: Dual-polarization observations of microbursts associated with intense convection: The 20 July storm during the MIST project. *Mon. Wea. Rev.*, **116**, 1521–1539, doi:10.1175/1520-0493(1988)116<1521:DPOOMA>2.0.CO;2.

——, C. J. Kessinger, and D. E. Kingsmill, 1994: Kinematic, thermodynamic, and visual structure of low-reflectivity microbursts. *Mon. Wea. Rev.*, **122**, 72–92, doi:10.1175/1520-0493(1994)122<0072:KTAVSO>2.0.CO;2.

Warning Decision Training Division, 2016: Convective storm structure and evolution. NOAA/NWS Warning Decision Training Division Radar and Applications Course 6, 592 pp. [Available online at http://wdtb.noaa.gov/courses/rac/documentation/rac17-severe.pdf.]

Whiton, R. C., P. L. Smith, S. G. Bigler, K. E. Wilk, and A. C. Harbuck, 1998: History of operational use of weather radar by U.S. weather services. Part II: Development of operational Doppler weather radars. *Wea. Forecasting*, **13**, 244–252, doi:10.1175/1520-0434(1998)013<0244:HOOUOW>2.0.CO;2.

Wilson, J. W., and R. M. Wakimoto, 2001: The discovery of the downburst: T. T. Fujita's contribution. *Bull. Amer. Meteor. Soc.*, **82**, 49–62, doi:10.1175/1520-0477(2001)082<0049:TDOTDT>2.3.CO;2.

Wurman, J., K. Kosiba, P. Markowski, Y. Richardson, D. Dowell, and P. Robinson, 2010: Finescale single- and dual-Doppler analysis of tornado intensification, maintenance, and dissipation in the Orleans, Nebraska, supercell. *Mon. Wea. Rev.*, **138**, 4439–4455, doi:10.1175/2010MWR3330.1.

Zrnić, D. S., and A. V. Ryzhkov, 1999: Polarimetry for weather surveillance radars. *Bull. Amer. Meteor. Soc.*, **80**, 389–406, doi:10.1175/1520-0477(1999)080<0389:PFWSR>2.0.CO;2.

——, ——, J. Straka, Y. Liu, and J. Vivekanandan, 2001: Testing a procedure for automatic classification of hydrometeor types. *J. Atmos. Oceanic Technol.*, **18**, 892–913, doi:10.1175/1520-0426(2001)018<0892:TAPFAC>2.0.CO;2.